Author's Accepted Manuscript

Effects of microstructures on fatigue crack initiation and short crack propagation at room temperature in an advanced disc superalloy

R. Jiang, N. Karpasitis, N. Gao, P.A.S. Reed

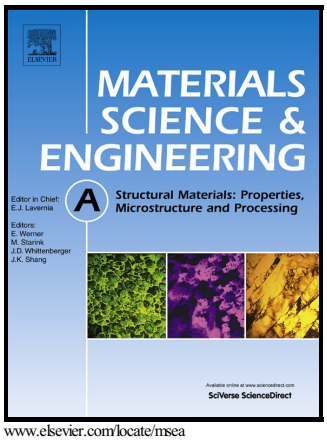

www.elsevier.com/locate/msea

PII: S0921-5093(15)30007-1
DOI: http://dx.doi.org/10.1016/j.msea.2015.05.065
Reference: MSA32393

To appear in: *Materials Science & Engineering A*

Received date: 11 December 2014
Revised date: 18 May 2015
Accepted date: 21 May 2015

Cite this article as: R. Jiang, N. Karpasitis, N. Gao and P.A.S. Reed, Effects of microstructures on fatigue crack initiation and short crack propagation at room temperature in an advanced disc superalloy, *Materials Science & Engineering A,* http://dx.doi.org/10.1016/j.msea.2015.05.065

This is a PDF file of an unedited manuscript that has been accepted for publication. As a service to our customers we are providing this early version of the manuscript. The manuscript will undergo copyediting, typesetting, and review of the resulting galley proof before it is published in its final citable form. Please note that during the production process errors may be discovered which could affect the content, and all legal disclaimers that apply to the journal pertain.

ACCEPTED MANUSCRIPT

Effects of microstructures on fatigue crack initiation and short crack propagation at room temperature in an advanced disc superalloy

R. Jiang*, N. Karpasitis, N. Gao, P. A. S. Reed

Materials Research Group, Engineering and the Environment, University of Southampton, Highfield, Southampton, SO17 1BJ, UK

*Corresponding author. Tel: +44 (0)23 80599450; Fax: +44 (0)23 80593016;

Email: Rong.Jiang@soton.ac.uk

Abstract

Fatigue crack initiation and early short crack propagation behaviour in two microstructural variants of a recently developed Low Solvus, High Refractory (LSHR) disc superalloy at room temperature has been investigated by three-point bending with replication procedure. The results shows that fine gained (FG) LSHR possesses higher fatigue life due to its better crack initiation resistance, limited crack coalescence and comparable Stage I crack propagation resistance to the coarse grained (CG) LSHR, although its resistance to Stage II crack propagation is inferior. Twin boundary (TB) cracking in the relatively large grains dominates the crack initiation process along with occasional crack initiation due to slip band cracking. Activation of the primary slip systems parallel to the TB at matrix and twin and high resolved shear stress associated with high Schmid factor (SF) are required for TB crack initiation. Cracks preferentially propagate along slip bands associated with high SF slip systems after initiation. But cracks also propagate along slip bands associated with slip systems with lower SF if the inclination angle between the slip band ahead of the crack tip and the crack segment of the crack tip is small enough to enable a steady transition (or non-deflected growth) of cracks across the grain boundary.

Keywords: Ni-based superalloys; twin boundary; Schmid factor; slip band; fatigue cracking

1. Introduction

Aeroengine turbine discs normally operate at elevated temperatures under dynamic loads in an aggressive service environment over significant periods of time. This requires disc materials to possess high strength at elevated temperatures, good fatigue and creep performance under these service conditions, and excellent oxidation and corrosion resistance. Powder metallurgy (PM) Ni-based superalloys have been widely used for aeroengine turbine

Accepted manuscript

ACCEPTED MANUSCRIPT

disc application due to their exceptional combined mechanical properties at elevated temperatures in combination with good oxidation/corrosion resistance [1-3]. Currently however, most of the disc alloys are designed for use at operating temperatures lower than 700^{o}C, beyond which severe environmental attack accelerated fatigue/creep failure may happen and thereby significantly reduces the service lifetime of the disc alloys [4].

In order to increase the operating temperature of disc alloys beyond 700 ^{o}C, to enhance fuel efficiency, produce higher thrust-to-weight ratio and reduce green-house gas emission, significant efforts have been made over past decades to develop more advanced disc alloys with superior tensile strength and fatigue/creep performance at elevated temperatures by optimizing alloy composition and controlling the material processing and heat treatment. It is well known that high temperature tensile strength and creep performance can be effectively improved by increasing the amount of γ' forming elements (such as Al and Ti) and refractory elements (such as W and Mo) to enhance precipitation strengthening and solid solution strengthening effects [2]. However, addition of these elements usually results in a high solvus temperature of γ', which makes the supersolvus and dual microstructure heat treatment challenging due to the significant grain growth and increased propensity of quench cracking caused by the greater residual thermal stress [5]. In order to neutralize the increase in γ' solvus temperature, relatively high Co content is used in more recent disc superalloys as it enables lowering of the γ' solvus temperature and introduce an additional strengthening effect by mechanical twinning during deformation, especially at temperatures above 650 ^{o}C [6, 7]. In fact, the Co content in these more recent disc alloys, such as RR1000, Rene' 104 and LSHR alloy, is about 5~7% higher compared with relatively older disc alloys, such as Udimet 720 and Waspaloy [3, 6, 8].

The LSHR alloy was recently developed for aeroengine turbine disc application by NASA. It combines the low solvus of Rene' 104 brought about by the high Co content and the high refractory element content of Alloy 10 [9]. Based on existing research carried out at NASA, it has been found that the LSHR alloy possesses exceptional high temperature tensile strength and creep resistance [6]. It is also claimed that the LSHR alloy has good processing versatility due to the low γ' solvus temperature, which makes it possible to produce a dual microstructure turbine disc with optimized creep and fatigue performance at various disc locations by differentiated heat treatments [6, 9, 10].

Accepted manuscript

ACCEPTED MANUSCRIPT

Studying low cycle fatigue (LCF) performance at elevated temperatures indicates that the typical fatigue-initiation sites and the overall fatigue life of LSHR alloy are related to the microstructures, test temperatures and strain ranges employed [6, 10]. Specifically, cracks mainly initiate from internal inclusions and/or pores and occasionally initiate from crystallographic facets in FG LSHR at elevated temperatures (427 ^{o}C and 704 ^{o}C). This has been observed when the applied total strain is less than 0.8% (which is usually associated with longer fatigue life). Whereas cracks predominantly initiate from crystallographic facets of larger grains in the CG LSHR variant, which usually produces a shorter fatigue life at similar moderate strain ranges [10]. When higher strain ranges were applied by conducting LCF tests at higher temperature (704 ^{o}C), an oxidation assisted crack initiation process was observed to come into effect, usually forming intergranular cracks, especially when a long dwell time was applied at the peak time during LCF tests [6]. The short crack propagation behaviour after initiation which is sensitive to the local microstructure adjacent to the crack tips was not investigated in these studies, and the intrinsic crack initiation process (in the absence of environmental attack) that is linked to the cyclic deformation processes at lower temperatures in the LSHR alloy has also not received much attention. It is generally accepted that fatigue crack initiation and short crack growth processes are important to optimise as they contribute to the majority of fatigue life of a turbine disc during service. This is due to the high overall component stresses which result in a relatively small extent of fatigue crack propagation prior to fast fracture and thereby limit the fatigue life dependency to the short crack growth regime [11-15]. As a result, a systematic assessment of crack initiation and subsequent short crack growth behaviour is necessary at both lower and elevated temperatures in order to evaluate the intrinsic (without environmental attack) and extrinsic (with environmental attack) fatigue crack processes in appropriate microstructural variants of the LSHR alloy. This is expected to provide a better understanding of the fatigue crack initiation and propagation processes and to contribute to the ongoing development of optimised disc alloys. It should also be noted that the bore region of a turbine disc will experience lower temperatures in service and optimisation of turbine alloys requires good fatigue resistance at both low and high temperatures. In this paper, crack initiation and subsequent short crack propagation behaviour in LSHR alloy at room temperature was investigated, and the effects of grain size, grain orientation and primary γ' precipitate distribution have been studied and are discussed. A companion study on crack initiation and short crack propagation in LSHR alloy at elevated temperatures will be presented in another paper.

Accepted manuscript

ACCEPTED MANUSCRIPT

2. Materials and experimental procedures

2.1 Materials

The LSHR alloy used in this study was provided by NASA. Composition (in wt.%) of the LSHR alloy is 12.5Cr, 20.7Co, 2.7Mo, 3.5Ti, 3.5Al, 0.03C, 0.03B, 4.3W, 0.05Zr, 1.6Ta, 1.5Nb, Ni bal. Specimens used for the short crack tests were extracted from a turbine disc which was fabricated by canning atomized LSHR alloy powder followed by hot isostatically pressing, extruding and isothermally forging. The extracted specimens were supersolvus heat treated at 1171 ^{o}C and subsolvus heat treated at 1135 ^{o}C to yield CG and FG microstructures respectively, followed by the same dual aging heat treatments [4]. The obtained microstructures are shown in Fig. 1, and the measured grain size and γ′ size are shown in Table 1. The details of microstructure evaluation can be found in our previous publication [4].

Table 1 Statistical data on size of grain, primary γ′ and secondary γ′ in LSHR alloy

Materials	Grain size (μm)	Primary γ′ (μm)	Secondary γ′ (nm)
CG LSHR	38.38±18.07	N/A	153± 29
FG LSHR	8.14±2.77	1.74±0.48	89± 15

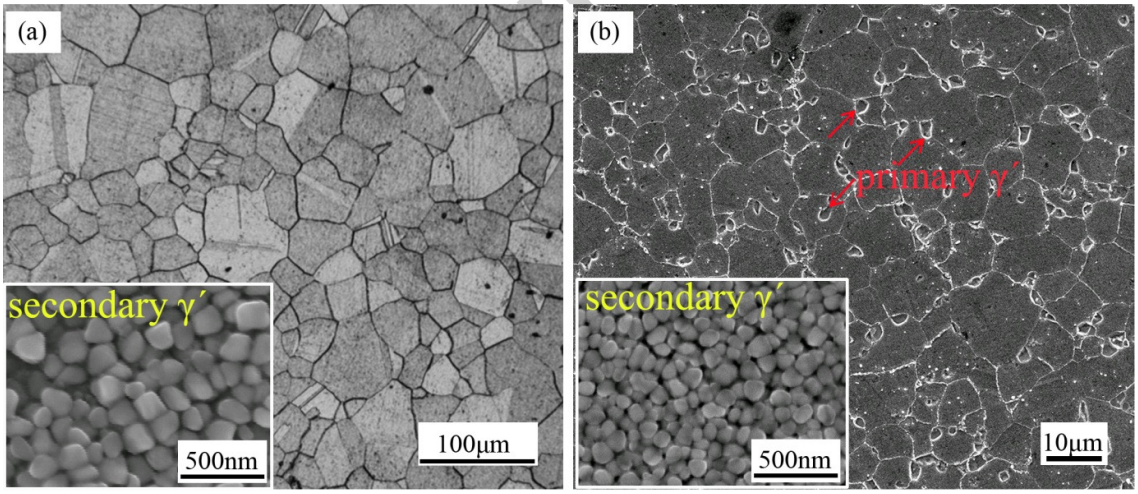

Fig. 1 Microstructures of (a) CG and (b) FG LSHR alloys obtained by supersolvus and subsolvus heat treatments respectively.

2.2 Experimental procedures

Fatigue tests were conducted on polished U-notch CG and FG LSHR specimens under three-point bend loading on an Instron 8501 hydraulic testing machine at room temperature

ACCEPTED MANUSCRIPT

with a 20 Hz sine waveform and a load ratio of 0.1. The applied load was calculated to produce a maximum nominal elastic stress of 1020 MPa at the notch root using simple elastic beam theory for the un-cracked ligament. The dimension of the U-notch specimen and the position of the loading rollers are shown in Fig. 2. The notch has a depth of 1.25 mm with a curvature radius of 2 mm. This notch type was chosen to provide an elastic stress concentration of around 2, i.e. representative of that seen in the fir tree root fixings used to secure blades to turbine discs. The notch was ground and then polished using dental felts by 1 μm diamond polishing paste before testing. Some of the tests were interrupted at certain intervals to make a replica of the notch root surface with a silicone compound (provided by Struers Ltd) to monitor crack evolution. Some tests were also halted before final failure to carry out more in-depth analysis of the crack growth morphology.

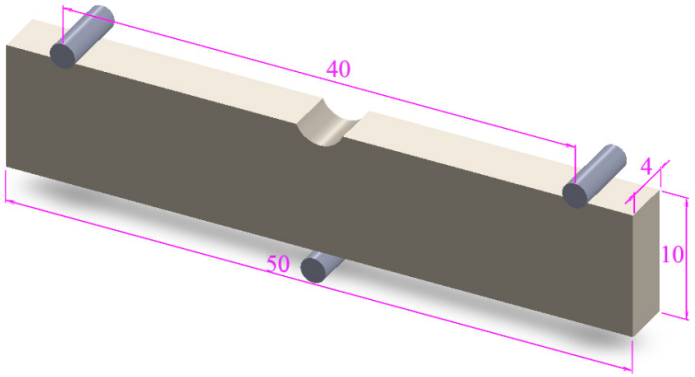

Fig. 2 Dimension of the U-notch specimen (in mm) and the positon of the loading rollers.

A JSM 6500 field emission gun scanning electron microscopy (SEM) was employed to examine the morphology of the fatigue fracture surface and notch root at an accelerating voltage of 15 kV. Optical microscopy (OM) was used to observe crack evolution on the replicas. Both actual crack length and projected crack length were measured with Image J software. Definition of actual and projected crack length is schematically shown in Fig. 3. In most cases, only those cracks were measured that grew relatively long (> 10 times the average grain size) and were still sufficiently isolated to be unaffected by the proximity of other cracks at the end of the test. Crack growth rate was derived by the secant method, and then was plotted against stress intensity factor range (ΔK).

Stress intensity factor values were calculated from the half surface crack length (c) using the empirical formula of Scott and Thorpe [16]. The interrupted CG LSHR specimen was metallographically sectioned and then the sectioned metallographic images were re-constructed in three dimensions (3D) using Avizo software to confirm the crack aspect ratio

ACCEPTED MANUSCRIPT

a/c (*a* is crack depth) to allow more accurate ΔK calculation as well as 3D crack tomography. During metallographic sectioning, micro-hardness indentions were introduced to the specimen surface to act as fiduciaries to align the 2D section images. The grinding/polishing depth was also estimated by the change of diagonal length of the indentions according to an established calibration. The stresses used for ΔK calculation were obtained by running elastic-plastic finite element modelling in Abaqus by simulating the loading roller with an appropriate pressure load and simulating the support roller with the restricted displacement in the vertical direction of the specimen. The contacting region with the rollers was assumed to be elastic to avoid non-convergence in the model.

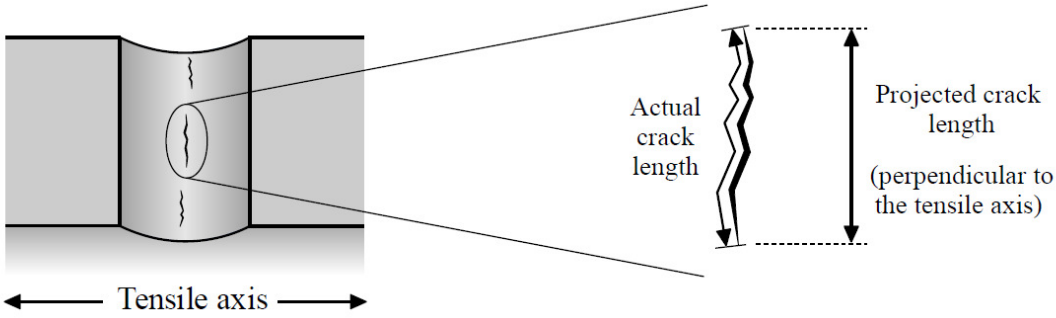

Fig. 3 Schematic diagram of the definition of actual and projected crack length.

Additional testing was conducted on a plain bend bar (PBB) specimen with a dimension of 4 mm × 4 mm × 50 mm under a maximum load of 1550 N along with the same replication procedures and crack length measurement approaches. The achieved maximum strain in the PBB specimen is slightly lower than that in the U-notch specimen (0.0067 vs. 0.0078) based on the simulation by finite element. This sample was used to evaluate the influence of grain orientation on crack initiation and early crack propagation by conducting electron backscatter diffraction (EBSD) analysis on the cracked regions at the centre of the top surface. The crack-initiating grain and early crack propagation region (in the CG LSHR) can be identified via surface observation in combination with replicas using OM. In addition, EBSD analysis was also conducted in the regions containing crack-initiating grains and secondary cracks in the FG LSHR fractured specimen. This was due to the fact that it is difficult to track the crack-initiating grain in the FG LSHR via surface observation in combination with replicas using OM due to the small grain size and the inability to use high magnification objective lenses in OM due to the notch geometry. A grain boundary tolerance angle of 2^{o} was employed for EBSD mapping. A step size of 1μm was used during the EBSD mapping for CG LSHR and a step size of 0.5 μm was used for FG LSHR. After EBSD indexing, Euler angles for grains

Accepted ma.

ACCEPTED MANUSCRIPT

containing crack segments and adjacent to crack path were extracted, and then the Schmid factor for the 12 primary slip systems (i.e. {111}<110>) in each grain was calculated according to the methodology presented in [17]. The slip traces corresponding to {111} slip planes in the cracked grains at the specimen surface were also calculated [18] and were used as a reference to identify the active slip systems associated with the actual crack segment within each cracked grain.

3. Results

3.1 Overall fatigue behaviour

Table 2 summarises the overall observations of the fatigue tests. As shown in the table, the fatigue life of the FG LSHR is nearly twice that of the CG LSHR for the U-notch specimens tested to failure. The equivalent estimated fatigue lifetime of the interrupted PBB specimen is higher than that of the U-notch specimen due to the absence of the stress concentration feature and the slightly smaller applied maximum strain. Crack initiation occurred after fewer cycles in the U-notch CG LSHR and a little later in the CG PBB specimen, as it took about 5000 and 10000 cycles respectively to produce observable cracks on replicas. Compared with the CG LSHR, FG LSHR possesses better crack initiation resistance indicated by the higher cycle number to first observable crack (denoted as fatigue crack initiation lifetime) and fewer cracks overall were observed at the end of the test. Observation of the fracture surfaces of the uninterrupted tests shows that the length of the crystallographic facets which are associated with Stage I crack propagation is approximately 10 times the average grain size in either the CG or FG LSHR variant according to 12 measurements made on the fracture surface in each case.

Table 2 Summary of the fatigue test results

Specimens	CG	CG	CG (PBB)	FG	FG
Test type	Tested to failure	Interrupted	Interrupted	Tested to failure	Interrupted
Fatigue lifetime/cycles at the end of the test	31482	26500	60000	57826	61500
Number of cycles to first observed crack		5000	10000		16000
Number of cracks at the end of the test		18	22		5
Extent of crystallographic faceting on fracture surface	333±38μm			105±15μm	

Accepted manuscript

ACCEPTED MANUSCRIPT

3.2 Fatigue crack initiation and propagation

Fig.4 presents the morphology of the fracture surfaces of the CG and FG LSHR U-notch tests. Crystallographic facets which are associated with slip band cracking can be seen in Fig.4 (a) and (d). Cracks initiate from crystallographic facets in both the CG or FG LSHR specimens, and the size of crack-initiating grains is usually larger than the average grain size. Cracks propagate along the crystallographic facets after initiation for a distance of about 10 times the average grain size until Stage II crack propagation sets in, forming a relatively flat feature on fracture surfaces as shown in Fig.4 (c) and (f). A secondary crack on the fracture surface can be discerned close to the crack initiation site in Fig.4 (b), and crack kinks which seem to be associated with crack deflection at TBs are observed on the crack path as indicated by the arrows. For the crack-initiating crystallographic facets in the FG LSHR, some of these are located next to primary γ′ as shown in Fig.4(d) and (e), although the role of primary γ′ in crack initiation is not clear. In addition, it seems that the FG LSHR possesses more crystallographic steps on the fracture surface, which is probably associated with the denser slip bands formed in the FG variant [19].

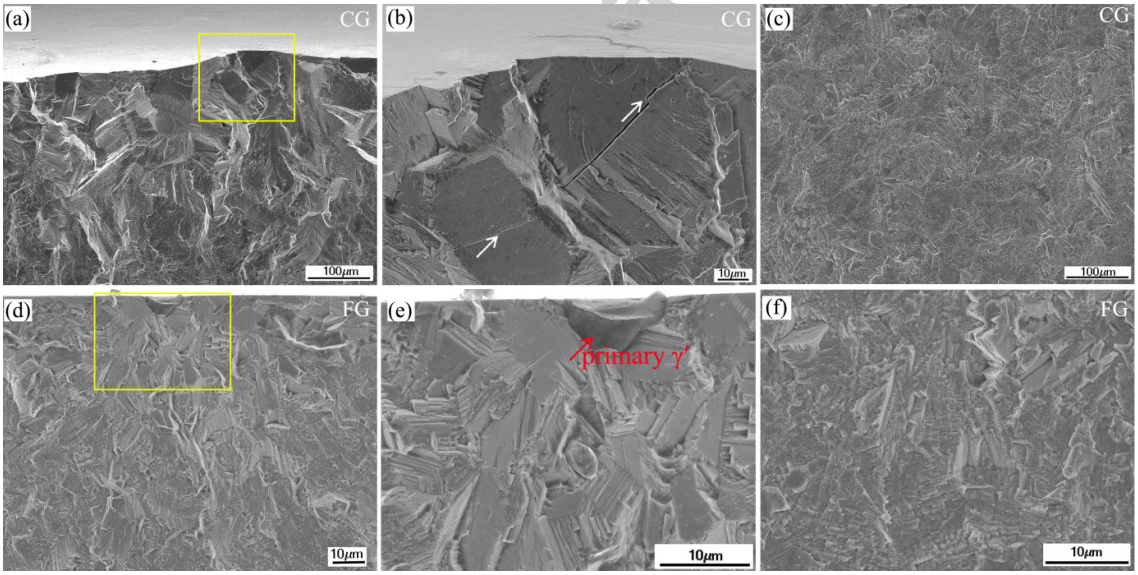

Fig.4 (a) and (d) Morphology associated with Stage I crack growth on fracture surfaces in the CG and FG LSHR; (b) and (e) close-ups of the regions highlighted in (a) and (d) respectively; (c) and (f) morphology associated with Stage II crack growth on fracture surfaces in the CG and FG LSHR.

ACCEPTED MANUSCRIPT

Interaction between the cracks and primary γ' was investigated by etching the microstructure in the notch in the interrupted FG LSHR specimen. As shown in Fig.5 (a), few primary γ' precipitates are cut by the crack path at the early crack propagation stage after initiation, except for one instance (indicated by the arrow). An occasional bowing of the crack path around a boride is observed as highlighted by the rectangle, and the crack by-passes the boride by cracking the interface of the matrix/boride. Some black replica silicone compounds remain around the crack after the replication process as they infiltrated into the crack and were difficult to remove. Fig.5 (b) and (c) shows the microstructure within the plastic zone ahead of the crack tip, within which intensive and intersecting slip bands in each grain can be clearly seen, indicating the occurrence of multiple slip. The slip bands usually terminate at grain boundaries or at the interfaces of γ matrix/primary γ'. Most of primary γ' precipitates within the plastic zone appear to be intact, indicating a beneficial effect of primary γ' on resisting crack propagation.

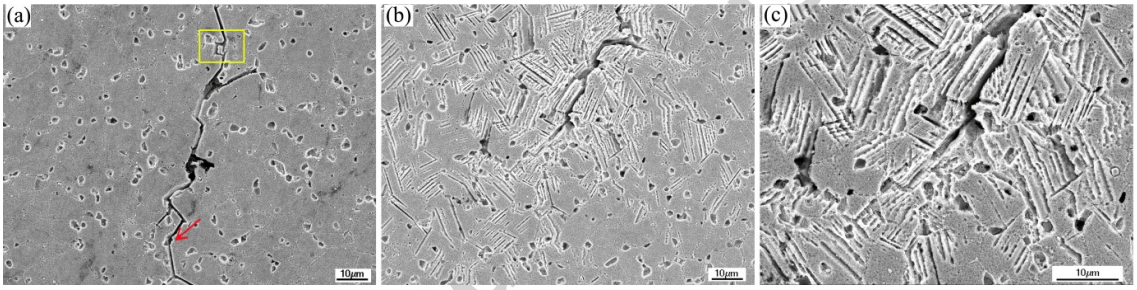

Fig.5 (a) Microstructure around crack path adjacent to crack initiation site in the FG LSHR; (b) microstructure ahead of crack tip in the FG LSHR and (c) high magnification of crack tip region shown in (b).

Evolution of the lengths (*2c*) of the primary cracks (i.e. the most fatal crack which caused failure) and the relatively isolated secondary cracks on the specimen surface in each interrupted test are presented in Fig.6 (a) and (b) respectively. The measured crack lengths corresponding to Stage I crack growth in the CG and FG LSHR based on the observation of fracture surfaces are multiplied by 2 times the reciprocal of the crack aspect ratio (a/c), and then are plotted in the figures as well. As shown in the graphs, accelerated and decelerated crack growth can be observed, and also crack arrest is discerned (e.g. CG C1a and CG C6a (PBB)). It is found that a crack propagates at a higher speed in the FG LSHR indicated by the steeper slope in the curve of crack length vs. loading cycle when the stage II crack propagation mode becomes dominant. Whilst it seems that the FG LSHR shows a comparable

crack growth to the CG LSHR during the stage I crack propagation period. For the CG LSHR, crack coalescence can be observed during crack propagation, which is rarely seen in the FG LSHR. However, the expected acceleration of crack propagation after coalescence is not always observed as demonstrated by the coalescence of crack CG C1b and CG C1c in the U-notch specimen and the coalescence of crack CG C6a (PBB) and CG C6b (PBB) in the PBB specimen. Fig. 6 (c) shows the evolution of the tortuosity (actual crack length/projected crack length) of the measured cracks, from which it can be found that the crack tortuosity is generally higher in the CG LSHR than that in the FG LSHR, even though the value of the tortuosity is quite scattered and varies from crack to crack.

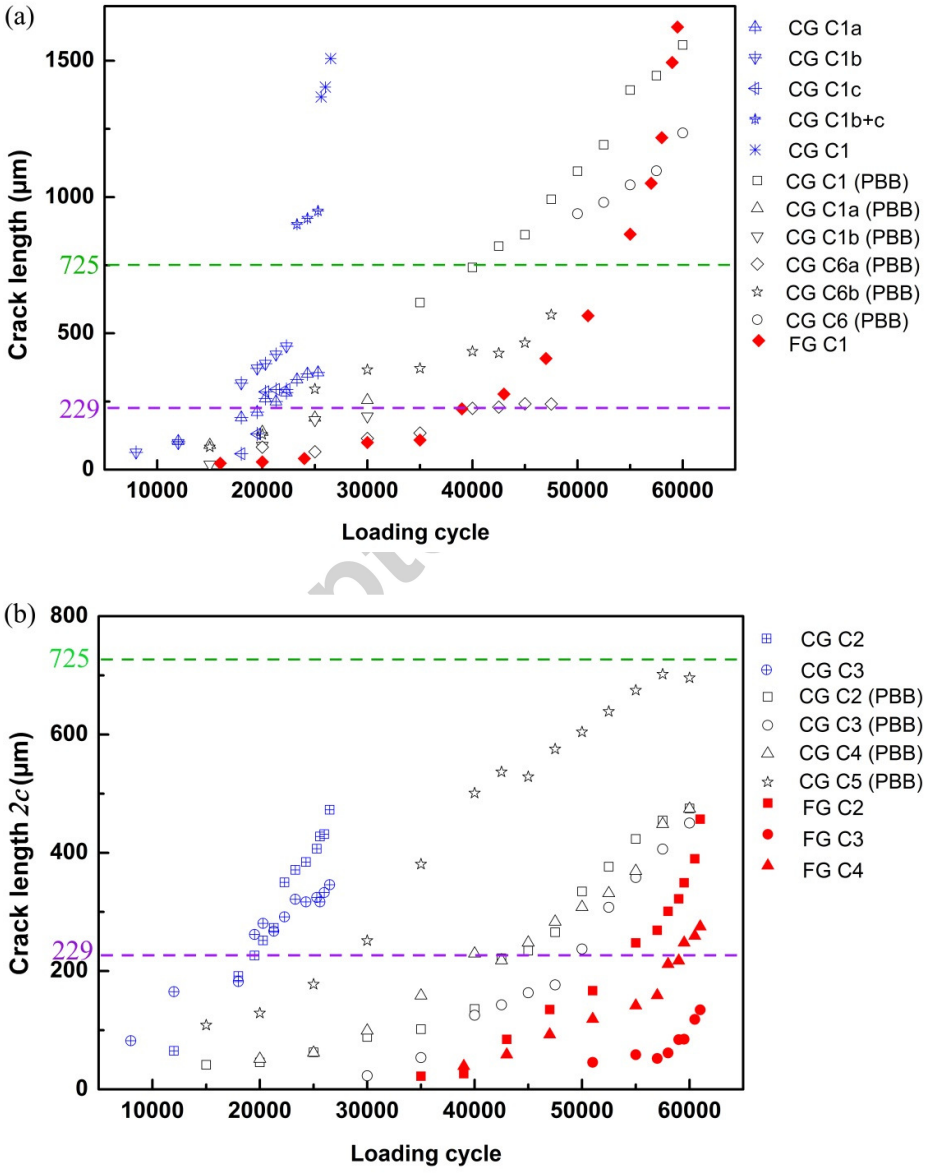

ACCEPTED MANUSCRIPT

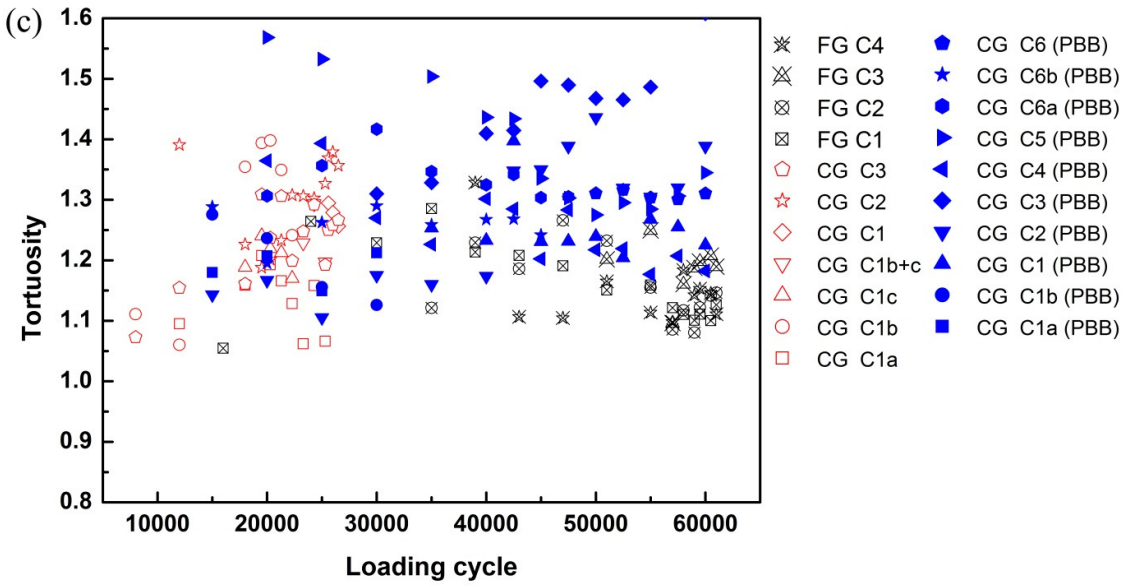

Fig.6 (a) Primary and (b) secondary crack length evolution in the interrupted tests for the CG and FG LSHR alloys; and (c) evolution of the tortuosity of the measured cracks.

Two metallographic sectioned slices and the overall 3D tomography of crack CG C1 in the U-notch interrupted specimen are presented in Fig.7. As shown in the microstructures around the crack path at the notch surface (Fig. 7(a)) and 28μm beneath notch surface (after removal of notch root material Fig. 7(b)), the crack coalescence sites can be clearly seen. Intensive slip bands are observed at the crack coalescence regions due to the interaction of the plastic zones of the two approaching cracks. A zig-zag crack path is discerned followed by a significant crack deflection at the crack tip of CG C1a at the notch surface (Fig.7 (a)) when the crack passes through a grain boundary. Similar zig-zag crack path and crack deflection are observed underneath the notch surface. Moreover, a marked inclination angle between the crack segments at the crack tip of CG C1a at notch surface and 28μm underneath notch surface can be seen from the inset SEM images, and such an inclination of crack plane in depth direction is probably correlated to the temporary crack arrest observed for crack CG C1a as shown in Fig. 6 (a). The obtained crack tomography is shown in a video in Fig.7 (c), from which the tortuous nature of the crack plane in 3D can be seen. Although the cracks CG C1a and C1b appear to coalesce at notch surface as shown in Fig.7 (a), they are still separated from each other underneath the notch surface as shown in the crack tomography. On the contrary, the cracks CG C1b and C1c coalesce at both surface and depth. The measured average aspect ratio of the crack from the crack tomography is 0.918, which was used for subsequent ΔK calibration. It should be noted here that the crack aspect ratio may vary from

specimen to specimen, and even vary from crack to crack in the same specimen. The crack aspect ratio of 0.918 (which is used for ΔK calculation of all the cracks of interest) is still an assumption for simplicity.

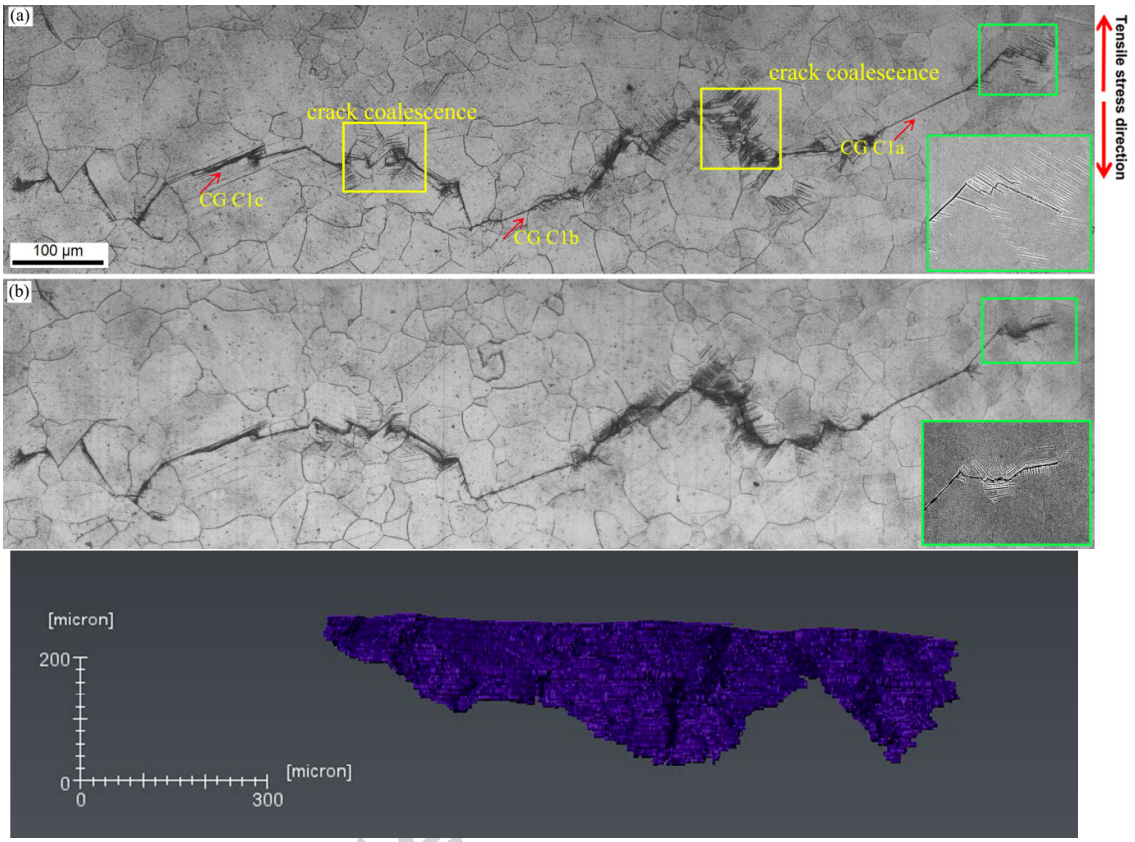

Fig.7 Microstructure around crack CG C1 at (a) the notch surface and (b) 28μm underneath the notch surface; and (c) tomography of CG C1.

Crack growth rate for each measured crack in the CG and FG LSHR are plotted against calculated ΔK as shown in Fig.8. The long crack growth rates along with the fitting lines according to the published Paris law behaviour [20] for both CG and FG LSHR at room temperature are also plotted for comparison with short crack growth behaviour. Typical small crack growth behaviour is seen, i.e. fluctuating crack growth rate and relatively higher crack growth rates at the same nominal ΔK compared to the established long crack data. This is clearly observed in both the CG or FG LSHR alloys at low ΔK level. It seems that the crack growth rates in the CG LSHR are more variable than in the FG LSHR, which may be related to the greater number of cracks and the more tortuous crack paths observed in the CG LSHR. At higher ΔK levels corresponding to longer crack lengths, the crack growth rates appear to lie closer to long crack growth data. The discrepancy between the crack growth rate at high

ΔK level for short and long cracks may arise from the difference in the specimen geometry overall constraint and employed load ratio [6]. Although the fatigue life of the FG LSHR is higher as shown previously in Table 2, the crack once initiated propagates at a higher speed in the FG LSHR, especially at the relatively high ΔK level for the small crack or long crack data. When ΔK level is low (~ <12MPa√m), the crack growth rate in the FG LSHR is comparable to that in the CG LSHR. Such crack growth behaviour indicates that the higher resistance to crack initiation and the equivalent resistance to early short crack propagation contribute to the higher fatigue lifetime observed in the FG LSHR test.

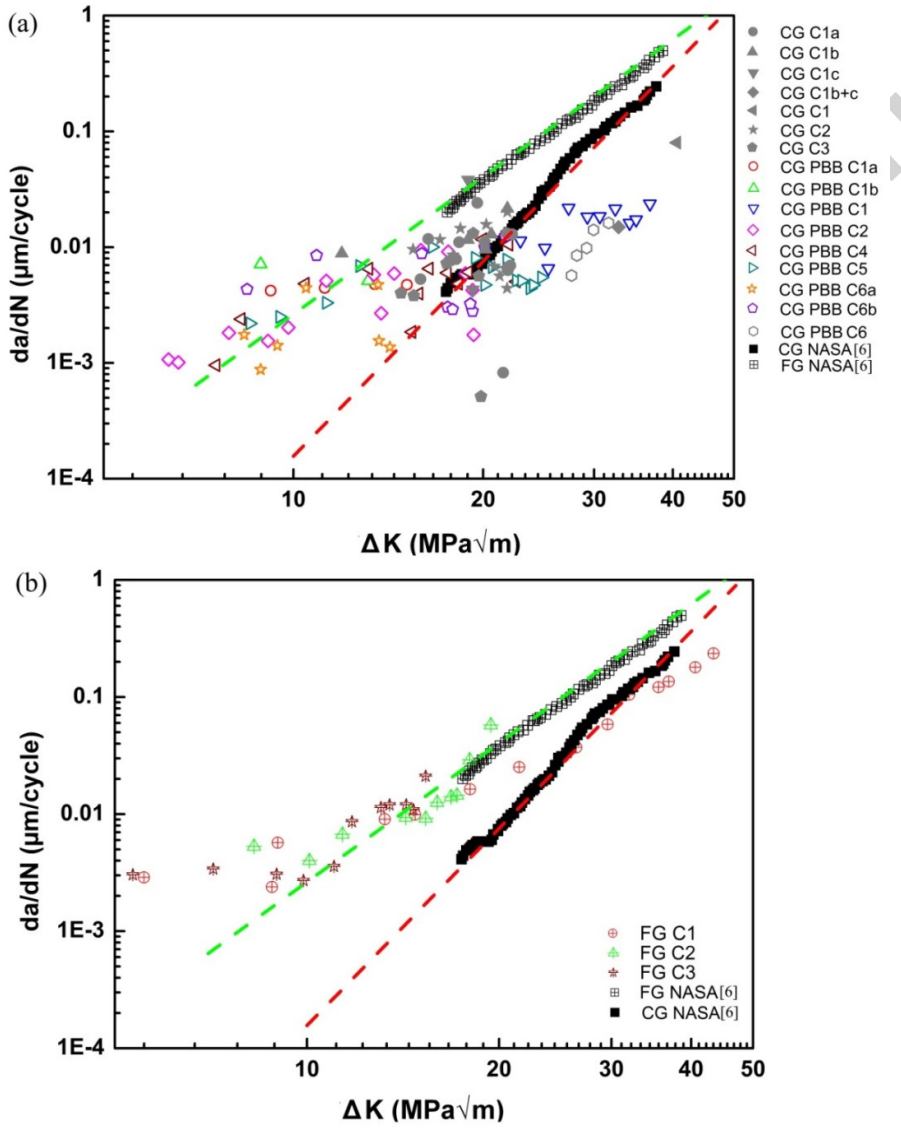

Fig.8 Crack growth rate in (a) CG and (b) FG LSHR alloys. The long crack growth rate of the LSHR alloy was extracted from NASA's report [6].

ACCEPTED MANUSCRIPT

3.3 Influence of grain orientation on crack initiation and propagation

EBSD analysis was conducted around the cracks (CG C1~C6 (PBB)) on the top central surface of the PBB specimen to particularly investigate the influence of grain orientation on crack initiation and early crack propagation processes. The PBB specimen orientation was selected to allow easier EBSD evaluation. The crack-initiating grains are identified by tracking down the cracks on the replicas to the stage just after initiation and then comparing the crack segment just after initiation on the replica and the corresponding area containing the crack path on the final investigated specimen surface.

Fig. 9 (a) shows the microstructure around crack CG C1 (PBB) and Fig.9 (b) shows the corresponding grain orientation map overlapped with the random high angle grain boundaries, special grain boundaries and crack paths. It is found that cracks initiate from TB in the relatively large grains as indicated by the arrows. Crack segments which are parallel to TB can also be observed during propagation. The same TB crack initiation was also observed in other cracked regions along with occasional crack initiation due to slip band cracking.

A summary of crack initiation sites from the EBSD investigation for the CG LSHR is presented in Table 3. The measured inclination angles (α_m) between the main crack segment and tensile stress axis within each crack-initiating grain are also listed in the table. By comparing the measured inclined angle with the calculated inclination angle (α_c) between the possible slip traces of the {111} slip planes and the tensile stress axis, it is possible to identify the active primary slip system associated with the crack segment. Additionally, the calculated SF (μ_c) for each active primary slip system associated with crack initiation and the highest SF (μ_h) in the crack- initiating grains are presented in the table as well. As shown in Table 3, cracks predominantly initiate from TB. The TBs and slip bands associated with crack initiation are usually associated with the primary slip system with the highest SF under the applied load conditions, and the SF of the active primary slip system is usually greater than 0.45. However, it is also found that some of the TBs associated with crack initiation are related to the slip systems with second highest SF. It appears that the slip traces in both matrix and twin corresponding to the primary slip systems associated with TB cracking have a similar inclination angle relative to tensile stress axis and parallel to the TB, although the SF of these slip systems is not always the highest within the crack-initiating grains. The slip traces corresponding to the highest SF slip systems in the twinning-related grains where crack CG C1a (PBB) and C6b (PBB) initiated are not parallel to the TB according to the calculated

Accepted manuscript

ACCEPTED MANUSCRIPT

inclination angle. These slip traces which are non-parallel to TB appear to be less favourable for crack initiation. It seems that high resolved shear stress acting on the primary slip systems indicated by high SF in matrix and twin simultaneously is not sufficient to initiate a crack at the TB, it still requires active primary slip systems parallel to the TB.

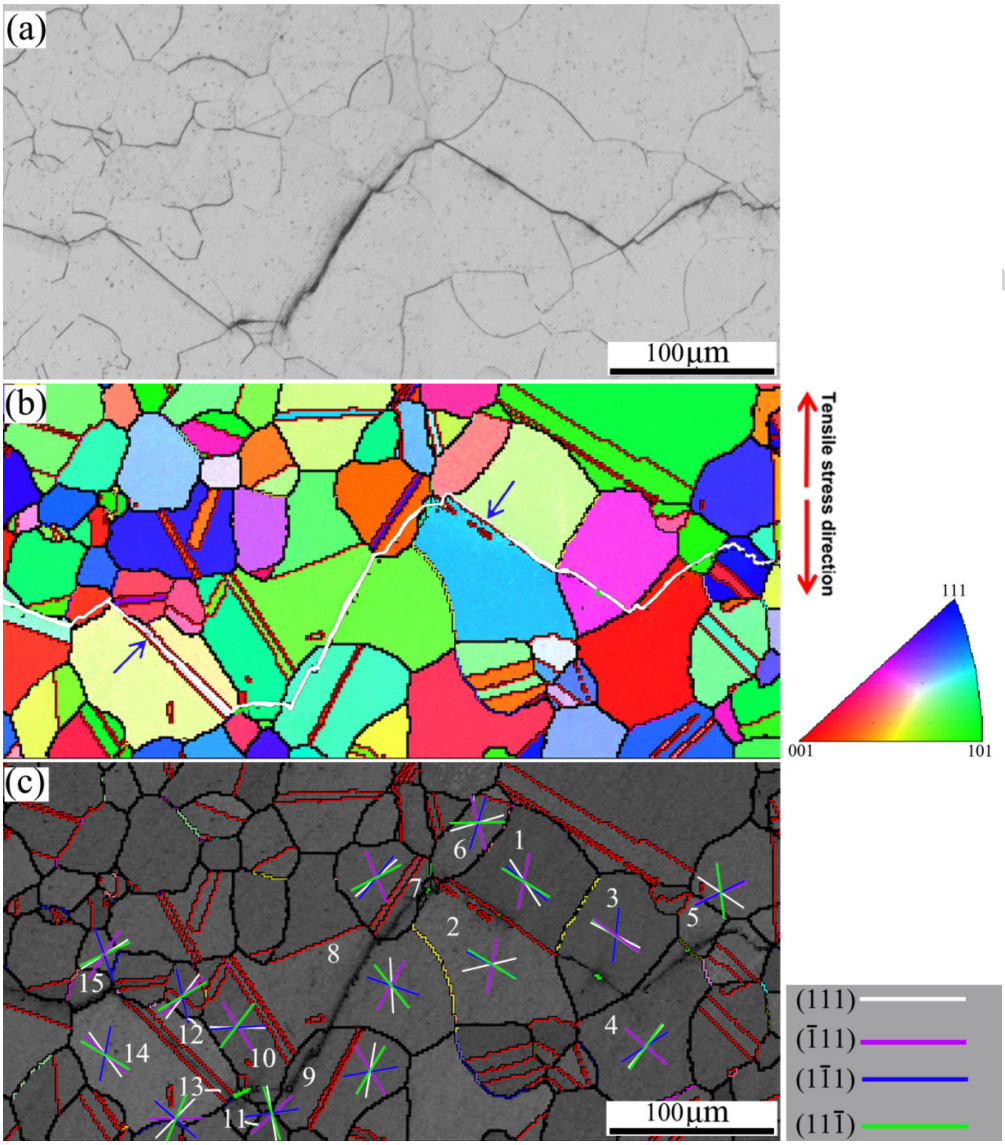

Fig.9 (a) Microstructure around crack CG C1 (PBB); (b) grain orientation map and (c) band contrast map around the crack CG C1 (PBB) overlapped with random high angle grain boundaries and special grain boundaries. Black lines in (b) and (c) represent the random high angle grain boundaries, and the red lines present the Σ3 twin boundaries. Crack path is outlined by white line in (b), and the calculated slip traces in the grains containing or adjacent to crack path are labelled in (c).

ACCEPTED MANUSCRIPT

Table 3 Summary of crack initiation sites in the interrupted test for CG PBB specimen

Crack ID	Crack initiation site	Crack-initiating grain size	Matrix/ Twin	μ_c	α_c	α_m	μ_h	β
C1a	TB	105.8	Matrix	0.451	121.2	121.5	0.494	130
			Twin	0.452	121.2		0.496	117
C1b	TB	84.5	Matrix	0.497	131.7	130	□	□
			Twin	0.495	131.3		□	□
C2	TB	37.9	Matrix	0.478	55.1	58.5	□	□
			Twin	0.479	55.7		□	□
C3	Slip band	111.4	/	0.489	131	130.2	□	□
C4	TB	75.9	Matrix	0.473	132	132.5	□	□
			Twin	0.471	132		0.476	126
C5	TB	101.9	Matrix	0.483	38.5	41.2	□	□
			Twin	0.488	39.3		□	□
C6a	TB	58.1	Matrix	0.490	51.6	50.8	□	□
			Twin	0.490	51.9		0.495	78.2
C6b	TB	109.2	Matrix	0.481	126	126.9	0.494	124
			Twin	0.480	126		0.492	116

Note: β is the calculated inclined angle between the tensile stress axis and the slip trace corresponding to the slip system with highest SF; □ means the SF of the slip system associated with crack initiation is the highest SF in the crack-initiating grain.

Fig.9 (c) presents the calculated slip traces for the {111} slip planes within the cracked grains near to crack initiation sites and grains adjacent to the crack path on the contrast band map with the overlapped grain boundaries. The ID of the investigated grains is also labelled in Fig. 9(c). Generally, the crack segment within each grain is parallel to one of the calculated slip traces, indicating TB and/or slip band cracking and the cracks propagating along the slip bands/TBs, even though there is a slight deviation between the calculated slip traces and the actual crack segments. The calculated inclination angle α_c and the measured inclination angle α_m along with the maximum SF of the slip systems on each {111} plane within investigated grains are listed in Table 4. Similar to crack initiations shown previously, it is found that the SF of the active primary slip system associated with the crack segment in each cracked grain is not always the highest under the investigated conditions.

Accepted manuscript

ACCEPTED MANUSCRIPT

Table 4 Summary of μ_c, α_c, and α_m in the grains containing or adjacent to crack path in the CG LSHR PBB specimen.

Grain ID	Slip system	μ_c	α_c	α_m	Grain ID	Slip system	μ_c	α_c	α_m
Grain 1	(111)[1-10]	0.257	147.0	121.5	Grain 9	(111)[01-1]	0.058	9.73	31.7
	(-111)[110]	0.141	11.6			(-111)[01-1]	0.348	149	
	(1-11)[011]	*0.494*	*129.9*			(1-11)[110]	0.261	79.9	
	(11-1)[011]	**0.451**	**121.2**			**(11-1)[1-10]**	**0.419**	**30.5**	
Grain 2	(111)[01-1]	0.276	76.6	72.1	Grain 10	(111)[1-10]	0.3061	90.9	85.9
	(-111)[01-1]	0.152	9.4			(-111)[110]	0.427	148.3	
	(1-11)[110]	*0.496*	*117.2*			**(1-11)[011]**	**0.449**	**85.7**	
	(11-1)[1-10]	**0.452**	**121.2**	121.5		*(11-1)[011]*	*0.470*	*37.6*	
Grain 3	(111)[10-1]	0.365	117.0	125.7	Grain 11	(111)[01-1]	0.032	170.2	45
	(-111)[110]	**0.496**	**126.0**			**(-111)[01-1]**	**0.478**	**46.7**	
	(1-11)[-101]	0.232	16.7			(1-11)[110]	0.381	81.7	
	(11-1)[1-10]	0.459	124. 6			(11-1)[1-10]	0.277	162.5	
Grain 4	(111)[1-10]	0.378	39. 2		Grain 12	(111)[10-1]	0.289	36.9	
	(-111)[01-1]	0.457	131.0	140		(-111)[110]	0.496	48.1	
	(1-11)[011]	**0.453**	**57.2**	56.3		(1-11)[-101]	0.145	167.6	
	(11-1)[1-10]	0.407	35.6			(11-1)[1-10]	0.446	59.3	
Grain 5	(111)[1-10]	0.408	124.4	66.8	Grain 13	(111)[1-10]	0.271	44.7	130
	(-111)[101]	**0.461**	**67.3**			(-111)[101]	0.476	89.1	
	(1-11)[110]	0.371	63.5			**(1-11)[110]**	**0.497**	**131.7**	
	(11-1)[101]	0.108	172.4			(11-1)[101]	0.349	22.6	
Grain 6	(111)[01-1]	0.396	73.4		Grain 14	(111)[10-1]	0.280	143.9	130
	(-111)[110]	0.173	165.1			**(-111)[110]**	**0.495**	**131.3**	
	(1-11)[110]	0.246	17.0			(1-11)[-101]	0.138	11.3	
	(11-1)[011]	0.197	88.7			(11-1)[1-10]	0.444	120.0	
Grain 7	(111)[1-10]	0.439	48.2	40.1	Grain 15	*(111)[10-1]*	*0.479*	*57.9*	64
	(-111)[110]	0.229	157.5			(-111)[110]	0.417	33.0	
	(1-11)[011]	**0.466**	**38.8**			(1-11)[110]	0.217	160.6	
	(11-1)[011]	0.420	62.5			**(11-1)[101]**	**0.429**	**65.8**	
Grain 8	(111)[01-1]	0.022	176.8	29.8					
	(-111)[01-1]	**0.310**	**29.1**						
	(1-11)[110]	0.359	109.1						
	(11-1)[1-10]	*0.470*	*141.4*						

Note: Active primary slip systems are highlighted by red bold font, and the slip systems associated with highest SF but not the active slip system are highlighted by blue italic font. The active slip systems related to crack deflection are highlighted by underlined green font.

As shown in Fig. 9(c), a small deflection occurs when the crack propagates into grain 3 just after initiation due to the similar inclination angle of the active primary slip system in grain 3 and the crack-initiating twinning-related grain. Significant deflection occurs when the crack propagates from grain 3 into grain 4 and from crack-initiating twinning-related grain into grain 7. The zig-zag crack path in grain 4 is associated with the two active primary slip systems with very similar values (the highest SF and the secondary highest SF shown in Table 4), which assists the occurrence of the deflection. The crack deflects at the boundary of

Accepted manuscript

ACCEPTED MANUSCRIPT

the crack-initiating twinning-related grain/grain 6 as the primary slip systems are not easily activated in grain 6 indicated by the relatively low SF. Therefore the crack propagates into grain 7 where the primary slip system with a relatively high SF is activated. Crack deflection within grain 2 associated with a slip system with lower SF occurs to facilitate the crack propagating into grain 7. Similar apparent deflections can also be observed when a crack propagates into nearby grains after initiation at the TB of grain 13/grain 14. Crack coalescence occurs at grain 8 (according to replica observations) where the active slip system is associated with relatively low SF but the resultant slip band is geometrically favourable for crack coalescence as it has a small inclination angle to both approaching crack segments in grain 7 and grain 9 respectively.

Figs. 10 (a) and (b) present the microstructure and contrast map along with possible slip traces for the region containing the crack-initiating grain in the FG LSHR. Table 5 summarises the calculated inclination angle α_c and the measured inclination angle α_m along with the maximum SF of the slip systems on each {111} plane within grains of interest. As shown in Fig. 10 (a), large crystallographic facet can be seen on the fracture surface, indicating the crack initiation region. Similar to observations in CG LSHR, the slip band (probably a TB) related to crack initiation in grain 1 (Fig. 10 (b)) at the notch root surface is not associated with the slip system with the highest SF as shown in Table 5, but it is parallel to the TB between grain 3/grain1 and the slip trace associated with the highest SF in grain 3. After initiation, the crack propagates into grain 2 without a deflection at the notch root surface as the slip band associated with activated slip system with the highest SF in grain 2 has the same orientation in relation to the crack segment in the crack-initiating grain. Primary γ′ precipitates which are located at the boundary of grain 1/grain 2 are observed next to the crack path. However, it should be noted that the primary γ′ precipitates and γ matrix are not distinguishable from each other for EBSD indexation as they have the same face centred cubic crystal structure and a similar lattice parameter. Therefore, primary γ′ precipitates appear as grains in the EBSD band contrast map.

Figs. 10 (c) and (d) show the microstructure and band contrast map with possible slip traces in cracked grains around a secondary crack adjacent to the fracture surface. Although the crack-initiating grain can not be identified directly in Fig. 10 (c), it is reasonable to infer that the crack may have initiated in grain 4 or grain 7 as labelled in Fig. 10 (d) as indicated by the greater opening width of the crack segments in these two grains, and it seems that the crack is more likely to have initiated in grain 4 due to the much larger grain size (compared

Accepted manuscript

ACCEPTED MANUSCRIPT

with grain 7) which is usually associated with crack initiation in polycrystalline Ni-based superalloys. As shown in Table 5, whether the crack initiates in grain 4 or grain 7, it is consistent with the previous observation in the CG LSHR concerning crack initiation at a TB where active slip systems are associated with high SF in the matrix/twin and parallel to the TB, or crack initiation at a slip band associated with the highest SF (the highest and second highest SF in grain 7 are nearly the same). In terms of crack propagation after initiation, crack segments which are parallel to the calculated slip traces can be found in grain 6, grain 8, grain 9, and grains 12-14. Some of these crack segments are associated with slip traces with the highest SF (i.e. in grain 8, grain 9 and grain 13), and some of these crack segments are associated with relatively low SF, such as grain 6, probably due to this enabling a minimisation of the inclination angle between crack segments in neighbouring grains or due to the existence of primary γ' at the boundary of grain 6. A significant crack deflection is observed in grain 9, and two crack segments in grain 9 are found to be parallel to the calculated slip traces. However, one main crack segment in grain 9 (as indicated by the arrow in Fig. 10 (c)) and crack segments in grains 10 and 11 are not closely linked to the calculated slip traces, which may be related to crack coalescence adjacent to grain 11. Similar observations are also found in grains 12 and 14 when the crack approaches another crack tip.

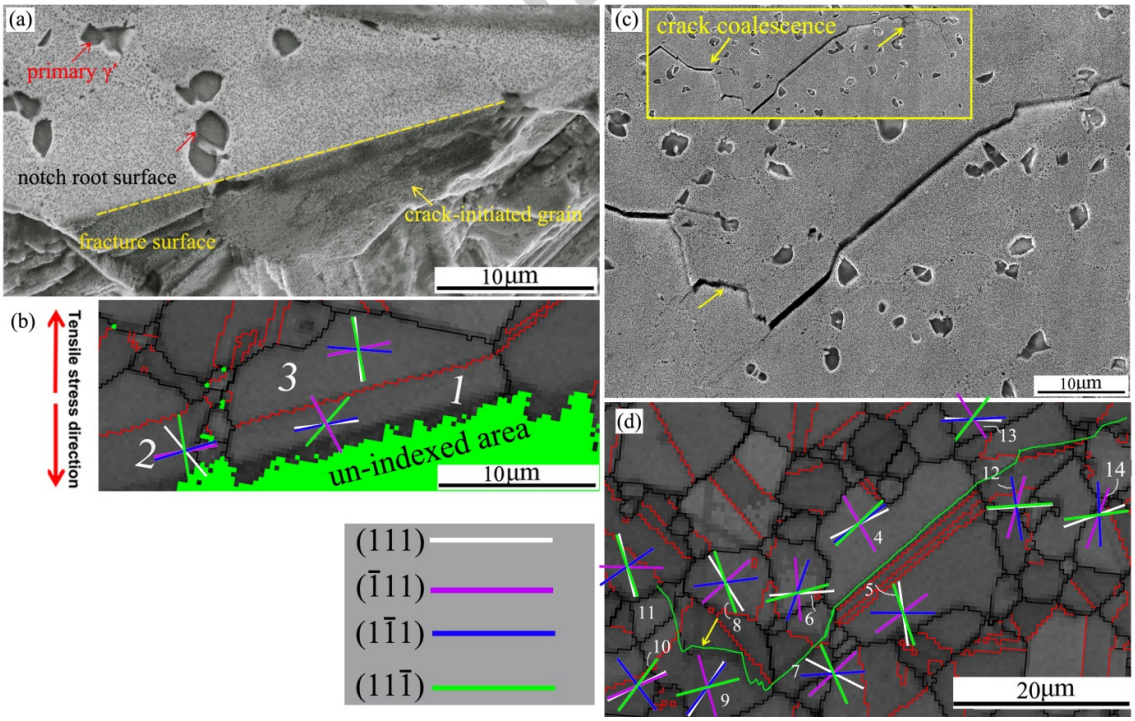

Fig. 10 (a) Microstructure around crack initiation region in the fractured FG LSHR; (b) band contrast map around the crack initiation region shown in (a); (c) microstructures around

ACCEPTED MANUSCRIPT

secondary cracks at the notch root surface in the fractured FG LSHR, and a low magnification shot of the full crack path with crack coalescence is inserted in the image; and (d) band contrast map around the secondary cracks shown in (c). Black lines in (b) and (d) represent the random high angle grain boundaries, and the red lines represent the Σ3 twin boundaries. The crack path is outlined by a green line in (d), and the calculated slip traces in the grains containing or adjacent to the crack path are labelled in (b) and (d) respectively.

Table 5 Summary of μ_c, α_c, and α_m in the grains containing or adjacent to crack path in the FG LSHR**.**

Grain ID	Slip system	μ_c	α_c	α_m	Grain ID	Slip system	μ_c	α_c	α_m
Grain 1	(111)[01-1]	0.291	83.6	75.2	Grain 8	(111)[1-10]	0.129	148	47.6
	(-111)[01-1]	0.387	152			**(-111)[01-1]**	**0.494**	**47.9**	
	(1-11)[110]	**0.467**	**78.3**			(1-11)[-101]	0.434	82.7	
	(11-1)[1-10]	*0.489*	*41.3*			(11-1)[101]	0.299	161	
Grain 2	(111)[1-10]	0.328	140	75.4	Grain 9	(111)[01-1]	0.139	33.2	
	(-111)[101]	**0.494**	**79.6**			**(-111)[01-1]**	**0.213**	**164**	166.8
	(1-11)[-101]	0.431	63.2			*(1-11)[011]*	*0.424*	*37.2*	39.7
	(11-1)[1-10]	0.140	171			(11-1)[011]	0.258	75.2	**107.2 (?)**
Grain 3	(111)[1-10]	0.068	174		Grain 10	(111)[10-1]	0.396	63.7	**168.7 (?)**
	(-111)[01-1]	*0.468*	*78.1*			(-111)[110]	0.424	67.1	
	(1-11)[011]	0.434	94.4			(1-11)[-101]	0.417	143	
	(11-1)[1-10]	0.149	169			*(11-1)[1-10]*	*0.425*	*36.9*	
Grain 4	(111)[01-1]	0.437	63.5	51.3	Grain 11	(111)[1-10]	0.126	166	**143.9 (?)**
	(-111)[01-1]	0.352	150			(-111)[101]	0.227	91.2	
	(1-11)[110]	**0.446**	**53.8**			*(1-11)[-101]*	*0.410*	*55.4*	
	(11-1)[1-10]	0.437	46.3			(11-1)[1-10]	0.286	161	
Grain 5	(111)[1-10]	0.061	172	51.3	Grain 12	*(111)[10-1]*	*0.432*	*86.3*	
	(-111)[01-1]	**0.444**	**53.3**			(-111)[110]	0.216	15.7	17.4
	(1-11)[011]	0.298	90.2			(1-11)[110]	0.122	170.7	**64.4 (?)**
	(11-1)[1-10]	0.287	161			(11-1)[101]	0.274	86.2	
Grain 6	*(111)[01-1]*	*0.485*	*86*	20.6	Grain 13	(111)[01-1]	0.412	92.3	83.7
	(-111)[110]	0.068	175			(-111)[01-1]	0.399	147.1	
	(1-11)[110]	**0.244**	**19.8**			**(1-11)[110]**	**0.430**	**86.7**	
	(11-1)[011]	0.415	74.8			(11-1)[1-10]	0.429	37.9	
Grain 7	(111)[1-10]	0.354	117	47.6	Grain 14	*(111)[10-1]*	*0.459*	*70.1*	**35.5 (?)**
	(-111)[01-1]	**0.483**	**47**			(-111)[110]	0.292	20.2	
	(1-11)[011]	*0.486*	*86.3*			(1-11)[110]	0.022	177.6	
	(11-1)[1-10]	0.343	156			**(11-1)[101]**	**0.331**	**82.3**	80.8

Note: Active primary slip systems are highlighted by red bold font, and the slip systems associated with highest SF but not the active slip system are highlighted by blue italic font. The active slip systems related to crack deflection are highlighted by underlined green font. The measured α_m with a "?" means that the smallest difference between α_m and α_c is greater than 15º.

Accepted manuscript

ACCEPTED MANUSCRIPT

4. Discussion

4.1 Factors controlling crack initiation

Cracks mainly initiate at stress concentration sites giving rise to strain localisation. It is widely observed that cracks initiate at slip bands close to TBs and/or TBs in the polycrystalline Ni-based superalloys due to their high slip planarity [11, 15, 21]. In this study, crack initiation predominantly occurs at TBs and occasionally occurs at slip bands in the relatively large grain in the LSHR alloy due to the relatively high volume fraction of TBs caused by the low stacking fault energy. Although primary γ′ was observed next to crack initiating sites in the FG LSHR, there is no evidence to show that primary γ′ has a direct influence on the crack initiation process. Moreover, FG LSHR appears to have a better resistance to crack initiation than CG LSHR indicated by the higher number of cycles to the first observed crack and the fewer cracks observed overall at the end of the interrupted tests.

The better crack initiation resistance in the FG LSHR is correlated to the more homogeneous slip/deformation behaviour. It is well known that grain size has an influence on the slip planarity of the Ni-based superalloys. The coarse grained microstructure is related to the enhanced slip planarity as it provides a longer free slip length for dislocations, and produces longer but more widespread slip bands associated with heterogeneous deformation compared with the fine grained counterpart [19, 22]. The long and widespread slip bands usually act as a favourable stress concentrator, and thereby cause significant strain localisation as more intense back-and-forth dislocation movement is expected to be confined within this region and more dislocations are expected to pile up within the long slip band. Consequently, cracks are inclined to initiate from these long, heterogeneous slip bands.

The presence of a TB further increases the heterogeneity of the slip band distribution, which enhances the strain localisation [23]. It is reported that slip bands parallel to a TB can form easily at the matrix and twin adjacent to the TB and concentrate at the TB due to the high elastic incompatibility stress which is induced to meet the requirement of the discontinuity of stress and displacement across the TB [15, 23]. The concentrated slip bands at the TB which are associated with strain localisation therefore lead to crack initiation at the TB or in the region adjacent to the TB.

The orientation of twin-containing grains in relation to the tensile stress axis is important for crack initiation as it determines the resolved shear stress acting on the primary slip systems. As shown in Table 3, the active slip systems for crack initiation in the twin-

Accepted manuscript

ACCEPTED MANUSCRIPT

containing grains are associated with the high resolved shear stress indicated by high SF and parallel to TB, which is consistent with Miao's study on polycrystalline nickel-based superalloy Rene´ 88DT [15]. However, it seems that activation of the primary slip systems which are parallel to the TB in the matrix and the twin is a more important prerequisite for TB crack initiation, because it is found that the active slip systems associated with crack initiation are not always experiencing the highest resolved shear stress as observed in crack CG C1a (PBB) in this study. It seems that having the active primary slip systems parallel to the TB and high resolved shear stress (indicated by high SF) together influence the crack initiation process. It can be therefore concluded that the factors controlling crack initiation in the LSHR alloy are the occurrence of large twin-containing grains and activation of the primary slip systems parallel to the TB in both matrix and twin.

4.2 Effects of microstructure on short crack propagation

After crack initiation, cracks mainly propagate along the slip bands and/or TBs associated with high resolved shear stress, which gives rise to crystallographic facets on fracture surface and zig-zag crack paths until Stage II crack propagation sets in. The crack growth rate after crack initiation in the CG and FG LSHR appears to be similar perhaps due to several competing effects operating simultaneously. It is well known that grain boundaries are effective barriers for slip transmission due to the elastic anisotropy and plastic incompatibility at these regions, and thereby are effective in hindering crack propagation, especially random high angle grain boundaries [17]. From this perspective, the FG LSHR is expected to have better crack propagation resistance due to its higher proportion of grain boundaries. Furthermore, the long, intense and widespread slip bands in the CG LSHR are associated with more dislocation pile ups at grain boundaries, which results in higher stress concentration and thereby activates dislocation sources in the adjacent grains, facilitating crack propagation [19, 22, 24]. However, the coarse grained microstructure is also likely exhibit enhanced slip planarity and hence slip reversibility, which usually produce less strain accumulation within the slip bands, leading to better intrinsic crack growth resistance [11, 14]. In addition, coarse grained microstructures are associated with more tortuous crack path (Fig. 6 (c)) due to more significant crack deflection when passing through grain boundaries, which may cause extrinsic shielding due to roughness induced closure and reduction in ΔK due to crack path deviation, both of which will reduce the effective ΔK driving crack propagation.

Accepted manuscript

ACCEPTED MANUSCRIPT

The existence of primary γ′ in the FG LSHR appears beneficial in improving the crack propagation resistance during Stage I crack propagation as the slip bands were observed to be terminated at grain boundaries and/or interfaces of γ matrix/primary γ′. Similar beneficial effect of primary γ′ on crack growth has also been observed in disc superalloy U720Li [11], although it is reported that some primary γ′ precipitates were cut by the crack. This was rarely seen in this study as indicated by the intact primary γ′ along the crack path and within the plastic zone ahead of the crack tip.

As cracks propagate along slip bands and/or TBs in both CG and FG LSHR during Stage I crack propagation, activation of the primary slip systems and formation of slip bands in the grains ahead of the crack tip are critical to crack propagation. High resolved shear stress is generally believed to facilitate the activation of the primary slip systems. Hence the slip systems with high SF are preferentially activated for crack propagation as shown in Tables 4 and 5. However, it is found that a crack does not propagate exclusively along slip bands with the highest SF primary slip systems according to this EBSD analysis. In some cases, the crack propagates along slip bands with a small inclination angle relative to the previous crack segment, although these slip bands are associated with relatively low SF slip systems as observed at grain 8 in Fig. 9 (c) where crack coalescence occurs. Similar short crack propagation along crystallographic facets associated with relatively low SF was also observed in other Ni-based superalloys [25].

It seems that geometrical compatibility of the overall 3D crack path is also an important influential factor when cracks propagate into adjacent grains which may be related to the energy required to produce new cracked surface [26, 27]. As shown in the crystallographic model proposed by Zhai et al. [26], the tilt angle of the traces of the crack-plane across a grain boundary at the surface and the twist angle of the crack-plane deflection at a grain boundary into the depth are the key factors that control the path and growth rate of a short crack. Large crack-plane twists and tilts when a crack passes through a grain boundary are usually required to fracture a large area at the grain boundary, which could result in crack arrest and/or branching. Conversely, a small crack-plane twist and tilt may enable continuous short crack growth across a grain boundary, which may be not necessarily related to the primary slip systems with highest SF. Although there is no detailed analysis of the crack-plane twist in depth in this study, one case shown in Fig. 7 demonstrates a temporary crack arrest of CG c1a due to the large inclination (or twist) in depth at the crack tip, which is consistent with Zhai's study. Moreover, the frequently observed zig-zag path which is

Accepted manuscript

ACCEPTED MANUSCRIPT

associated with duplex slip band cracking when a crack propagates through a grain boundary could also provide an example of the crack geometrical compatibility as the zig-zag crack path is believed to minimize the energy required to rip open the grain boundary [25, 27].

4.3 Effect of microstructure on fatigue lifetime

Fatigue lifetime is controlled by the fatigue crack initiation lifetime and the crack propagation lifetime. As discussed preciously, the FG LSHR possesses better crack initiation resistance and equivalent resistance to Stage I crack propagation but relatively inferior resistance to Stage II crack propagation compared with the CG LSHR. Although the number of cycles to first observed crack is higher in the FG LSHR compared with the CG variant, the difference in crack initiation lifetime between these two LSHR variants only contributes to a small part of the difference in the fatigue lifetime. In light of the equivalent resistance to stage I crack propagation but relatively inferior resistance to stage II crack propagation in the FG LSHR, it is believed that much higher fatigue lifetime in the FG LSHR is associated with the far fewer cracks formed. Due to the existence of a large number of cracks in the CG LSHR, frequent crack coalescence occurred during crack propagation, which significantly accelerated the fracture process, although the deceleration of crack propagation caused by the shielding effect of approaching/neighbouring cracks has been reported in some other metallic materials [28, 29].

Apart from the grain size and primary γ', secondary and tertiary γ' precipitates also have an influence on crack initiation and propagation processes, which further influences the fatigue lifetime. Depending on the size of secondary and tertiary γ' precipitates, dislocations have to bypass the γ' by shear cutting or Orowan looping mechanism during deformation [2], which influences the slip planarity and thereby influences the crack initiation resistance in Ni-based superalloys. In addition, the size and volume fraction of secondary and tertiary γ' precipitates usually influence the strength of Ni-based superalloys which is closely related to the strain damage in an individual loading cycle. In this study, the higher fatigue lifetime in the FG LSHR probably also arises from its relatively higher strength brought about by the finer grains and secondary γ'. However, it is difficult to quantify the contribution of secondary and tertiary γ' precipitates to the fatigue lifetime of the LSHR alloy due to the variation in size and volume fraction of secondary and tertiary γ' precipitates in this study. Further study concerning the fatigue crack initiation and propagation behaviour in the LSHR alloy by controlling the microstructural variables independently will be helpful to understand

Accepted manuscript

ACCEPTED MANUSCRIPT

the influence of secondary and tertiary γ′ precipitates on slip character and low temperature fatigue resistance.

5. Conclusions

The influence of microstructures on crack initiation and early short crack propagation was assessed by three-point bend loading with a replication procedure in combination with OM, SEM and EBSD observation. Based on the aforementioned results and discussion, the following conclusions can be made:

(1) FG LSHR alloy possesses a higher fatigue life due to its better fatigue crack initiation resistance and equivalent resistance to Stage I crack propagation compared with the CG LSHR, even though its resistance to Stage II crack propagation is inferior. Frequent crack coalescence occurs in the CG LSHR due to the existence of a large number of cracks, which significantly accelerates the fatigue fracture process and results in a shorter fatigue lifetime. Primary γ′ precipitates improve the resistance to crack propagation in the FG LSHR to some extent as the slip bands usually terminate at grain boundaries or interfaces of γ matrix/primary γ′.

(2) Cracks mainly initiate from TBs and occasionally initiate from slip bands in relatively large grains with favourable orientation in relation to the tensile stress axis. TB crack initiation is closely related to the activation of the primary slip systems parallel to TB at matrix and twin. These active slip systems are associated with high resolved shear stress indicated by relatively high SF.

(3) Cracks propagate along slip bands/TBs during Stage I giving rise to crystallographic facets on fracture surfaces. Stage II crack propagation sets in after crack propagates along crystallographic facets by a distance of ~10 times the average grain size. crack propagation during Stage I is usually associated with the slip band cracking which correlates to slip systems with high SF. Duplex slip band cracking along slip systems with similar SF occurs to facilitate crack deflection or to allow a crack to pass through the grain boundaries.

Acknowledgement

The authors would like to thank the University of Southampton, UK and the China Scholarship Council, China, for financial support. NASA (particularly Tim Gabb) is thanked for supplying the LSHR alloy.

Accepted manuscript

ACCEPTED MANUSCRIPT

Reference

[1] J. Guedou, J. Lautridou, Y. Honnorat, Journal of Materials Engineering and Performance, 2 (1993) 551-556.
[2] R.C. Reed, The Superalloys: Fudamentals and applications, Cambridge University Press, (2006).
[3] D. Furrer, H. Fecht, Journal of the Minerals, Metals and Materials Society, 51 (1999) 14-17.
[4] R. Jiang, S. Everitt, M. Lewandowski, N. Gao, P.A.S. Reed, International Journal of Fatigue, 62 (2014) 217-227.
[5] J. Gayda, P. Kantzos, J. Miller, Journal of Failure Analysis and Prevention, 3 (2003) 55-59.
[6] T. P. Gabb, J. Gayda, J. Telesman, NASA report NASA/TM-2005-213645, (2005).
[7] Y. Yuan, Y.F. Gu, T. Osada, Z.H. Zhong, T. Yokokawa, H. Harada, Scripta Materialia, 66 (2012) 884-889.
[8] J. Telesman, T. P. Gabb, A. Garg, P. Bonacuse and J.Gayda, TMS Superalloy 2008. Warrendale (PA): The Minerals, Metals & Materials Society, (2008) 807~816.
[9] J. Gayda, T. P. Gabb, J. Gayda, TMS Superalloy 2004. Warrendale (PA): The Minerals, Metals & Materials Society, (2004) 323-340.
[10] T.P. Gabb, P.T. Kantzos, J. Telesman, J. Gayda, C.K. Sudbrack, B. Palsa, International Journal of Fatigue, 33 (2011) 414-426.
[11] H.T. Pang, P.A.S. Reed, International Journal of Fatigue, 30 2009-2020.
[12] M. Goto, D. M. Knowles, Engineering Fracture Mechanics, 60 (1998) 1-18.
[13] H.T. Pang, P.A.S. Reed, International Journal of Fatigue, 25 (2003) 1089-1099.
[14] H.T. Pang, P.A.S. Reed, Materials Science and Engineering: A, 448 (2007) 67-79.
[15] J. Miao, T.M. Pollock, J. Wayne Jones, Acta Materialia, 57 (2009) 5964-5974.
[16] P.M. Scott, T.W. Thorpe, Fatigue & Fracture of Engineering Materials & Structures, 4 (1981) 291-309.
[17] W.Z. Abuzaid, M.D. Sangid, J.D. Carroll, H. Sehitoglu, J. Lambros, Journal of the Mechanics and Physics of Solids, 60 (2012) 1201-1220.
[18] P. Villechaise, L. Sabatier, J.C. Girard, Materials Science and Engineering: A, 323 (2002) 377-385.
[19] D. Krueger, S. Antolovich, R. Stone, Metallurgical and Materials Transactions A, 18 (1987) 1431-1449.
[20] S. Suresh, Fatigue of Materials, Cambridge University Press, (2004).
[21] R.R. Stephens, L. Grabowski, D.W. Hoeppner, International Journal of Fatigue, 15 (1993) 273-282.
[22] S.F. Toh, W.M. Rainforth, Materials Science and Technology, 12 (1996) 1007-1014.
[23] L.L. Li, P. Zhang, Z.J. Zhang, H.F. Zhou, S.X. Qu, J.B. Yang, Z.F. Zhang, Acta Materialia, 73 (2014) 167-176.
[24] R. Keller, W. Zielinski, W.W. Gerberich, Materials Science and Engineering: A, 113 (1989) 267-280.
[25] W. Schaef, M. Marx, H. Vehoff, A. Heckl, P. Randelzhofer, Acta Materialia, 59 (2011) 1849-1861.
[26] T. Zhai, A.J. Wilkinson, J.W. Martin, Acta Materialia, 48 (2000) 4917-4927.
[27] T. Zhai, X.P. Jiang, J.X. Li, M.D. Garratt, G.H. Bray, International Journal of Fatigue, 27 (2005) 1202-1209.
[28] B. Stokes, N. Gao, P.A.S. Reed, Materials Science and Engineering: A, 445–446 (2007) 374-385.
[29] B. Stokes, N. Gao, P.A.S. Reed, K.K. Lee, Metallurgical and Materials Transactions A, 36 (2005) 977-988.

Accepted manuscript